A modified generalized Bloch-mode synthesis for the efficient modeling of periodic structures using the wave-based finite element method

Vinícius Mauro de Souza Santos [1,2], **Thiago de Paula Sales** [1], **Morvan Ouisse** [2]
[1] Aeronautics Institute of Technology, Mechanical Engineering Division,
Praça Marechal Eduardo Gomes 50, Vila das Acácias, São José dos Campos, Brazil
e-mail: **vinicius.santos@ga.ita.br**

[2] SUPMICROTECH, Université de Franche-Comté, CNRS, Institut FEMTO-ST,
F-25000, Besançon, France

Abstract
Periodic structures have been attracting increasing interest due to their potential for manipulating waves. The Wave-based Finite Element Method (WFEM) is typically employed to model such systems, involving the examination of a finite element mesh of a single unit cell of the periodic lattice. However, the utilization of the WFEM with more challenging problems, encompassing unit cell models with several degrees of freedom, can be challenging, as it involves operating with large-sized matrices. To tackle this matter, one developed a modified generalized Bloch-mode synthesis that, in conjunction with the WFEM, can efficiently and accurately model periodic structures. Simulations were performed on a plate-like elastic metamaterial, where relative errors between resonances of the reduced model and the reference solution less than 0.5% and cross signature scale factor close to one across frequency were found, demonstrating the outstanding performance of the MGBMS and WFEM in computing dispersion curves, wave shapes, and forced responses.

1 Introduction

Periodic structures are defined as those systems that exhibit geometric or material periodicity [1, 2]. They manifest in various engineering structures, such as airplane fuselages, rotating machines, pipeline systems, and numerous other examples. Interestingly, they can exhibit several phenomena that can be used as innovative solutions in engineering [3, 4]. For instance, periodic structures may reveal phenomena such as waveguiding [5], cloaking [6], Anderson's localization [7], confinement [8], negative refraction index [9], non-reciprocity [10], mode conversion [11], bandgap formation [12], and more.

The mathematical modeling of periodic structures can be approached in various ways, such as the Finite Element Method (FEM) [13, 14], Wave-based FEM (WFEM) [15, 16], Plane Wave Expansion (PWE) [17, 18], Extended PWE (EPWE) [19, 20], Spectral Element Method (SEM) [21, 22] and Bloch-Floquet-based techniques [23, 24, 25, 26]. Among them, the WFEM is well recognized as an efficient numerical method for analyzing complex periodic structures [27, 28], including, e.g., phononic crystals (PCs) and elastic metamaterials (EMs) in general. By employing the WFEM, the dynamic behavior of periodic structures can be investigated by analyzing a finite element (FE) mesh of a single unit cell within its lattice. This wave-based modeling procedure significantly reduces computational time during subsequent calculations compared to the standard finite element method (FEM) [29], where the number of degrees of freedom (DoFs) is related to the quantity of unit cells in the periodic system.

However, the utilization of the WFEM may become very challenging when analyzing PCs and EMs in the mid- to high-frequency bands, where a fine mesh is required, resulting in FE models that can reach millions of DoFs. The application of the WFEM can also be challenging for unit cell FE models with several boundary

DoFs, as the calculation of eigenvalues and eigenvectors, utilized to compute forced responses for a finite system, involves operating with matrices of order dependent on the number of boundary equations. To tackle this matter, and therefore, speed up the analysis of periodic structures using the WFEM, it is of utmost importance to consider size-reduced unit cell FE models, obtained through model order reduction (MOR). They can be obtained by resorting to Component Mode Synthesis (CMS)-based approaches, inspired by the seminal works published in the sixties by Hurty [30], and Craig and Bampton [31], as well as by using system-/local-level characteristic constraint (S-CC or L-CC) modes [23, 24].

Krattiger and Hussein [23] developed an ultrafast strategy for elastic band-structure calculations called Bloch mode synthesis (BMS), where both boundary and interior DoFs of unit cells of periodic structures are represented as a set of reduced, yet accurate, modal DoFs. Interior DoFs are expressed as a combination of fixed interface modes and constraint modes, whereas boundary DoFs are reduced using S-CC interface reduction — a procedure which is applied after enforcing the Bloch-Floquet boundary conditions (BCs), and therefore becomes frequency-dependent. Four years later, Krattiger and Hussein introduced a novel MOR approach to compute dispersion curves of periodic systems called Generalized BMS (GBMS) [24]. Within this approach, the interior DoFs of unit cell FE models are reduced as in BMS, and the boundary DoFs are represented as a linear combination of interface/local vibration modes using L-CC MOR, prior to enforcing the Bloch-Floquet periodicity conditions, thereby avoiding the frequency dependence encountered in BMS.

More recently, Aladwani [32] extended the BMS method to electroelastic metamaterials with piezoelectric resonant shunt damping. The BMS technique was further developed by Aladwani et al. [33] for application to generally damped phononic materials, resorting to the classical state-space formulation. Van Belle et al. [34] employed the GBMS to accelerate the calculation of dispersion curves of a two-dimensional EM. Cool et al. [35] applied the BMS and GBMS methods to compute vibro-acoustic dispersion curves of periodic structures in a solid-air medium. Xi and Zheng [36] proposed improvements to the GBMS method by exploiting algebraic condensation, introducing the GBMS with algebraic condensation (GBMS-AC). Cool et al. [37] investigated the impact of the unit cell choice on the computational efficiency of band structure calculations using the GBMS. Van Belle et al. [38] used the GBMS method with substructuring to compute the forced response of a plate-type metamaterial. Zhu et al. [39] developed the Improved GBMS, employing algebraic condensation (IGBMS-AC). Jiang et al. [28] devised the Hybrid BMS (HBMS) MOR technique by considering hybrid Bloch-Floquet BCs.

The developments reported so far concerning the use of reduced models following the BMS and its variant approaches primarily focus on the analysis of PCs and EMs by examining dispersion curves. However, in real-life scenarios, structures are not infinite as implied by the Bloch-Floquet theorem. Hence, calculation of forced responses is a fundamental task to investigate wave propagation characteristics in finite periodic structures. Accordingly, in this work, we introduce a new version of the GBMS, denoted as Modified GBMS (MGBMS), which differs from the method developed by Krattiger and Hussein [24] in two aspects: (1) interface modes are calculated for the unit cell at a global level, and therefore, a frequency-based truncation criterion is effective in delimiting the space of the lowest frequency eigenvectors utilized to locally reduce boundary DoFs via L-CC MOR; (2) the Modal Assurance Criterion (MAC) is employed to remove redundant equations from the L-CC projection matrix while respecting the periodicity condition between adjacent unit cells required by the Bloch-Floquet theorem. Unit cell modal models, reduced as done in the MGBMS, can then be invoked in the WFEM, facilitating the analysis of wave propagation throughout periodic structures.

Figure 1 summarizes the main steps to model periodic structures using the MGBMS and WFEM efficiently. In summary, internal and boundary DoFs of a unit cell in a periodic structure are first reduced using the Craig-Bampton (CB) and L-CC MOR methods. Following the WFEM procedures, dispersion curves can be calculated, proceeded by the computation of forced responses, harmonic deformed patterns, and other results of interest for a finite periodic system. The numerical simulations presented afterward consider the application of the MGBMS and the WFEM to a plate-type EM assuming one-dimensional wave propagation behavior. However, the method is general and can potentially be applied to various periodic systems.

In the remainder of this paper, theoretical aspects relevant to the research work are summarized, including a detailed exposition about unit cell model reduction and a brief review related to the WFEM. Subsequently, results from numerical simulations are presented, followed by a summary of our findings and conclusions. Acknowledgments and references are provided at last.

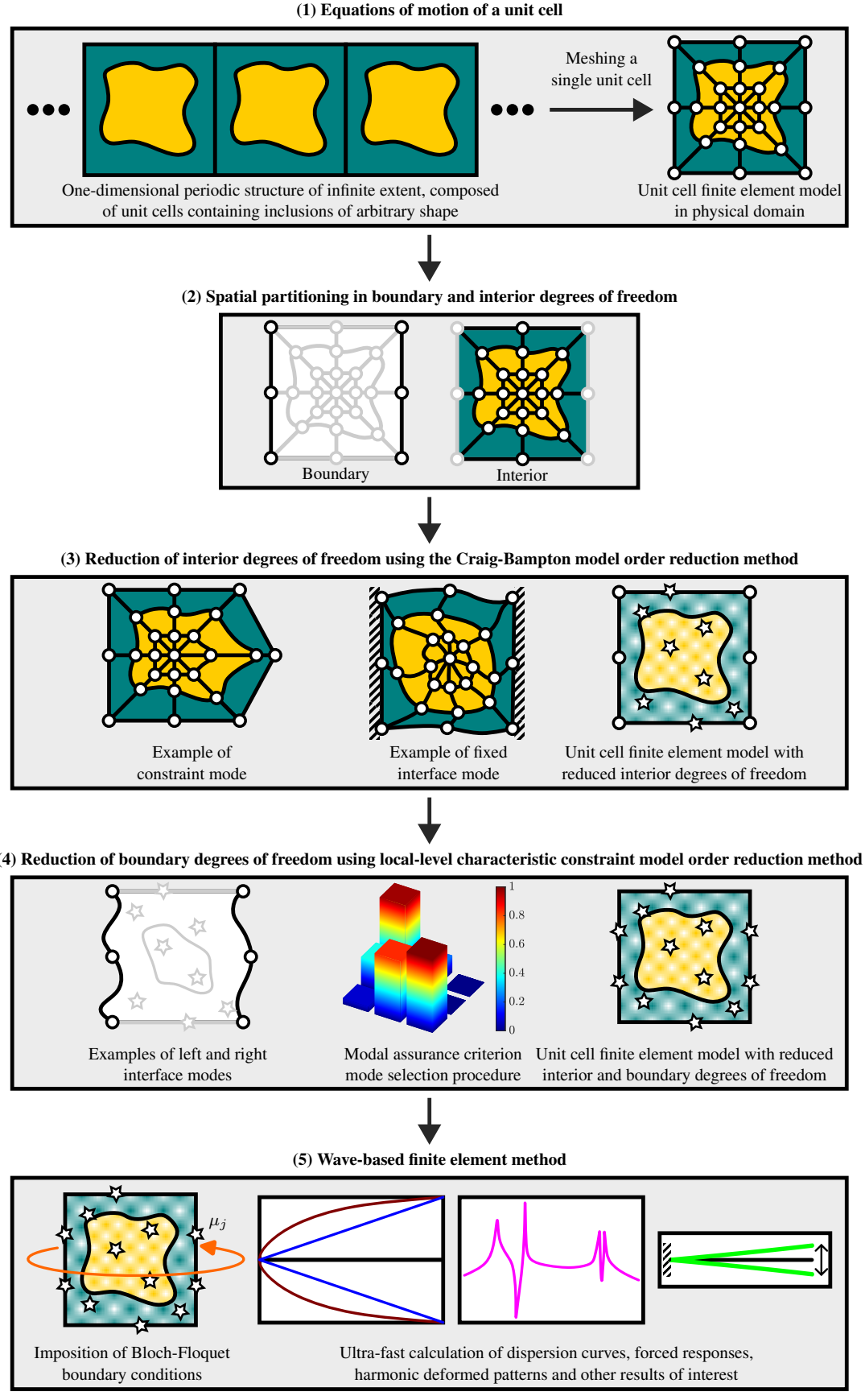

Figure 1: Flowchart illustrating the various steps employed for the ultra-fast analysis of periodic structures.

2 Modeling

The following subsections summarize the mathematical developments necessary for the efficient and accurate modeling of periodic structures using MGBMS and the one-dimensional WFEM. They cover the mathematical modeling of unit cells of periodic structures using FEM, topics related to the reduction of interior and boundary DoFs following the MGBMS, and a review of fundamental aspects related to WFEM, focusing on the calculation of wave modes and the computation of forced responses.

2.1 Equations of motion of a unit cell

As depicted in step **(1)** of Fig. 1, the first task for the efficient modeling of periodic structures using MGBMS and WFEM consists of identifying the smallest repeating structure of the periodic lattice, called unit cell. This unit cell can be spatially discretized using any discretization method, such as the FEM. Thereafter, following the WFEM, the related DoFs and load vectors, $\hat{\mathbf{q}}$ and $\hat{\mathbf{f}}$, respectively, can be labeled according to their locations within the cell, i.e., left (L), internal (I), and right (R), as illustrated in Fig. 2.

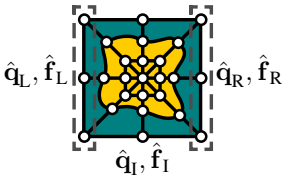

Figure 2: Mesh of a unit cell of a periodic structure with degrees of freedom and load vectors labeled.

The resulting set of discretized undamped equations of motion (EoMs), which describe the dynamic behavior of the unit cell, can be written as:

$$\begin{bmatrix} \hat{\mathbf{M}}_{\mathrm{LL}} & \hat{\mathbf{M}}_{\mathrm{LR}} & \hat{\mathbf{M}}_{\mathrm{LI}} \\ \hat{\mathbf{M}}_{\mathrm{RL}} & \hat{\mathbf{M}}_{\mathrm{RR}} & \hat{\mathbf{M}}_{\mathrm{RI}} \\ \hat{\mathbf{M}}_{\mathrm{IL}} & \hat{\mathbf{M}}_{\mathrm{IR}} & \hat{\mathbf{M}}_{\mathrm{II}} \end{bmatrix} \begin{Bmatrix} \ddot{\hat{\mathbf{q}}}_{\mathrm{L}}(t) \\ \ddot{\hat{\mathbf{q}}}_{\mathrm{R}}(t) \\ \ddot{\hat{\mathbf{q}}}_{\mathrm{I}}(t) \end{Bmatrix} + \begin{bmatrix} \hat{\mathbf{K}}_{\mathrm{LL}} & \hat{\mathbf{K}}_{\mathrm{LR}} & \hat{\mathbf{K}}_{\mathrm{LI}} \\ \hat{\mathbf{K}}_{\mathrm{RL}} & \hat{\mathbf{K}}_{\mathrm{RR}} & \hat{\mathbf{K}}_{\mathrm{RI}} \\ \hat{\mathbf{K}}_{\mathrm{IL}} & \hat{\mathbf{K}}_{\mathrm{IR}} & \hat{\mathbf{K}}_{\mathrm{II}} \end{bmatrix} \begin{Bmatrix} \hat{\mathbf{q}}_{\mathrm{L}}(t) \\ \hat{\mathbf{q}}_{\mathrm{R}}(t) \\ \hat{\mathbf{q}}_{\mathrm{I}}(t) \end{Bmatrix} = \begin{Bmatrix} \hat{\mathbf{f}}_{\mathrm{L}}(t) \\ \hat{\mathbf{f}}_{\mathrm{R}}(t) \\ \hat{\mathbf{f}}_{\mathrm{I}}(t) \end{Bmatrix}, \tag{1}$$

where $\hat{\mathbf{M}}_{ij}$ and $\hat{\mathbf{K}}_{ij}$ are the mass and stiffness matrices, respectively, with i and j accounting for the DoFs locations introduced in Fig. 2, i.e., L, R, and I; $\hat{\mathbf{q}}_j(t)$ represents time-dependent vectors of DoFs for the unit cell, possibly collecting displacements and rotations in the general case; $\hat{\mathbf{f}}_j(t)$ are the corresponding time-dependent load vectors encompassing forces and moments; and $\dot{(\,)}$ denotes time derivatives.

Seeking to introduce the MOR theory afterwards, in Subsections 2.2 and 2.3, Eq. (1) can be rewritten in a more convenient way, respecting the partitioning of DoFs into boundary and internal quantities [40], as illustrated in step **(2)** of Fig. 1:

$$\hat{\mathbf{M}} \begin{Bmatrix} \ddot{\hat{\mathbf{q}}}_{\mathrm{B}}(t) \\ \ddot{\hat{\mathbf{q}}}_{\mathrm{I}}(t) \end{Bmatrix} + \hat{\mathbf{K}} \begin{Bmatrix} \hat{\mathbf{q}}_{\mathrm{B}}(t) \\ \hat{\mathbf{q}}_{\mathrm{I}}(t) \end{Bmatrix} = \begin{Bmatrix} \hat{\mathbf{f}}_{\mathrm{B}}(t) \\ \hat{\mathbf{f}}_{\mathrm{I}}(t) \end{Bmatrix}, \tag{2}$$

where B collects boundary DoFs, i.e., $\mathrm{B} \in \{\mathrm{L}, \mathrm{R}\}$, and therefore:

$$\hat{\mathbf{M}} = \begin{bmatrix} \hat{\mathbf{M}}_{\mathrm{BB}} & \hat{\mathbf{M}}_{\mathrm{BI}} \\ \hat{\mathbf{M}}_{\mathrm{IB}} & \hat{\mathbf{M}}_{\mathrm{II}} \end{bmatrix}, \qquad \hat{\mathbf{K}} = \begin{bmatrix} \hat{\mathbf{K}}_{\mathrm{BB}} & \hat{\mathbf{K}}_{\mathrm{BI}} \\ \hat{\mathbf{K}}_{\mathrm{IB}} & \hat{\mathbf{K}}_{\mathrm{II}} \end{bmatrix}, \qquad \hat{\mathbf{q}}_{\mathrm{B}}(t) = \begin{Bmatrix} \hat{\mathbf{q}}_{\mathrm{L}}(t) \\ \hat{\mathbf{q}}_{\mathrm{R}}(t) \end{Bmatrix}, \qquad \hat{\mathbf{f}}_{\mathrm{B}}(t) = \begin{Bmatrix} \hat{\mathbf{f}}_{\mathrm{L}}(t) \\ \hat{\mathbf{f}}_{\mathrm{R}}(t) \end{Bmatrix}. \tag{3}$$

2.2 Model reduction of interior degrees of freedom

In accordance with step **(3)** of Fig. 1, the next task for achieving efficient modeling of periodic structures involves reducing interior DoFs using the CB MOR method [23, 24, 30, 31, 40, 41], while preserving boundary

equations. This can be accomplished by establishing the following transformation matrix:

$$\begin{Bmatrix} \hat{\mathbf{q}}_{\mathrm{B}}(t) \\ \hat{\mathbf{q}}_{\mathrm{I}}(t) \end{Bmatrix} = \mathbf{T}_{\mathrm{CB}} \begin{Bmatrix} \hat{\mathbf{q}}_{\mathrm{B}}(t) \\ \mathbf{q}_{\mathrm{I}}(t) \end{Bmatrix} = \begin{bmatrix} \mathbf{I} & \mathbf{0} \\ \boldsymbol{\Gamma} & \boldsymbol{\Xi} \end{bmatrix} \begin{Bmatrix} \hat{\mathbf{q}}_{\mathrm{B}}(t) \\ \mathbf{q}_{\mathrm{I}}(t) \end{Bmatrix}, \tag{4}$$

where $\mathbf{q}_{\mathrm{I}}$ represents a set of reduced internal modal DoFs; $\boldsymbol{\Xi}$ is the matrix of fixed interface modes, obtained by solving $(\hat{\mathbf{K}}_{\mathrm{II}} - \kappa_j \hat{\mathbf{M}}_{\mathrm{II}})\boldsymbol{\xi}_j = \mathbf{0}$ for the low-frequency eigenvectors; and $\boldsymbol{\Gamma}$ is the matrix of constraint modes, given by $\boldsymbol{\Gamma} = -\hat{\mathbf{K}}_{\mathrm{II}}^{-1}\hat{\mathbf{K}}_{\mathrm{IB}}$.

Accordingly, the reduced set of EoMs describing the dynamic behavior of the unit cell, with internal DoFs reduced by the CB MOR method and boundary DoFs preserved, can be written as:

$$\bar{\mathbf{M}} \begin{Bmatrix} \ddot{\hat{\mathbf{q}}}_{\mathrm{B}}(t) \\ \ddot{\mathbf{q}}_{\mathrm{I}}(t) \end{Bmatrix} + \bar{\mathbf{K}} \begin{Bmatrix} \hat{\mathbf{q}}_{\mathrm{B}}(t) \\ \mathbf{q}_{\mathrm{I}}(t) \end{Bmatrix} = \begin{bmatrix} \mathbf{I} & \boldsymbol{\Gamma}^{\mathrm{T}} \\ \mathbf{0} & \boldsymbol{\Xi}^{\mathrm{T}} \end{bmatrix} \begin{Bmatrix} \hat{\mathbf{f}}_{\mathrm{B}}(t) \\ \hat{\mathbf{f}}_{\mathrm{I}}(t) \end{Bmatrix}, \tag{5}$$

where $\bar{\mathbf{M}} = \mathbf{T}_{\mathrm{CB}}^{\mathrm{T}}\hat{\mathbf{M}}\mathbf{T}_{\mathrm{CB}}$, $\bar{\mathbf{K}} = \mathbf{T}_{\mathrm{CB}}^{\mathrm{T}}\hat{\mathbf{K}}\mathbf{T}_{\mathrm{CB}}$, and $(\ )^{\mathrm{T}}$ is the transpose operator.

2.3 Model reduction of boundary (interface) degrees of freedom

Even after performing the reduction of internal DoFs, excessive number of boundary equations might hinder the application of the WFEM. Therefore, reducing the boundary DoFs is a crucial task for efficiently modeling periodic structures, as illustrated in step **(4)** of Fig. 1. Therefore, the following projection holds:

$$\begin{Bmatrix} \hat{\mathbf{q}}_{\mathrm{B}}(t) \\ \mathbf{q}_{\mathrm{I}}(t) \end{Bmatrix} = \mathbf{T}_{\text{L-CC}} \begin{Bmatrix} \mathbf{q}_{\mathrm{B}}(t) \\ \mathbf{q}_{\mathrm{I}}(t) \end{Bmatrix} = \begin{bmatrix} \mathbf{L} & \mathbf{0} \\ \mathbf{0} & \mathbf{I} \end{bmatrix} \begin{Bmatrix} \mathbf{q}_{\mathrm{B}}(t) \\ \mathbf{q}_{\mathrm{I}}(t) \end{Bmatrix}, \tag{6}$$

where $\mathbf{L}$ is a block diagonal matrix, with two submatrices $\boldsymbol{\Psi}_{\mathrm{LR}} = [\boldsymbol{\psi}_{\mathrm{L}} \ \ \tilde{\boldsymbol{\psi}}_{\mathrm{R}}]$ lying along its diagonal, with $\boldsymbol{\psi}_{\mathrm{L}}$ and $\tilde{\boldsymbol{\psi}}_{\mathrm{R}}$ determined by obtaining the low-frequency eigensolutions of the following eigenvalue problem:

$$\left(\bar{\mathbf{K}} - \gamma_j \bar{\mathbf{M}}\right) \boldsymbol{\psi}_j = \mathbf{0}, \tag{7}$$

$$\boldsymbol{\Psi} = \begin{bmatrix} \boldsymbol{\psi}_{\mathrm{L}1} & \boldsymbol{\psi}_{\mathrm{L}2} & \boldsymbol{\psi}_{\mathrm{L}\ldots} \\ \boldsymbol{\psi}_{\mathrm{R}1} & \boldsymbol{\psi}_{\mathrm{R}2} & \boldsymbol{\psi}_{\mathrm{R}\ldots} \\ \boldsymbol{\psi}_{\mathrm{I}1} & \boldsymbol{\psi}_{\mathrm{I}2} & \boldsymbol{\psi}_{\mathrm{I}\ldots} \end{bmatrix} = \begin{bmatrix} \boldsymbol{\psi}_{\mathrm{L}}{}^{\mathrm{T}} & \boldsymbol{\psi}_{\mathrm{R}}{}^{\mathrm{T}} & \boldsymbol{\psi}_{\mathrm{I}}{}^{\mathrm{T}} \end{bmatrix}^{\mathrm{T}}. \tag{8}$$

In particular, $\tilde{\boldsymbol{\psi}}_{\mathrm{R}}$ is determined from the set of mode partitions gathered in $\boldsymbol{\psi}_{\mathrm{R}}$, for which the MAC number between $\boldsymbol{\psi}_{\mathrm{L}i}$ and $\boldsymbol{\psi}_{\mathrm{R}i}$, given by [42]:

$$\mathrm{MAC}\left(\boldsymbol{\psi}_{\mathrm{L}i}, \boldsymbol{\psi}_{\mathrm{R}i}\right) = \frac{\left|\boldsymbol{\psi}_{\mathrm{L}i}^{\mathrm{T}}\, \boldsymbol{\psi}_{\mathrm{R}i}^{*}\right|^2}{\left(\boldsymbol{\psi}_{\mathrm{L}i}^{\mathrm{T}}\, \boldsymbol{\psi}_{\mathrm{L}i}^{*}\right)\left(\boldsymbol{\psi}_{\mathrm{R}i}^{\mathrm{T}}\, \boldsymbol{\psi}_{\mathrm{R}i}^{*}\right)}, \tag{9}$$

is lower than a user-defined threshold value. In the equation above, $|\ |$ denotes the absolute value of a scalar and $(\ )^*$ the complex conjugate of a vector. This procedure is of utmost importance when applying the reduction of boundary DoFs, as it reduces the number of redundant equations utilized in the L-CC projection matrix. Such unnecessary equations usually lead to numerical issues when calculating forced responses for a finite periodic system using the WFEM, if not appropriately removed from the projection basis. To ensure that $\boldsymbol{\Psi}_{\mathrm{LR}}$ is not singular, it can be orthogonalized via QR or singular value decomposition [24].

Therefore, the EoMs for the unit cell, reduced through L-CC MOR after its internal DoFs have been represented in modal coordinates using the CB method, can be expressed as:

$$\mathbf{M} \begin{Bmatrix} \ddot{\mathbf{q}}_{\mathrm{B}}(t) \\ \ddot{\mathbf{q}}_{\mathrm{I}}(t) \end{Bmatrix} + \mathbf{K} \begin{Bmatrix} \mathbf{q}_{\mathrm{B}}(t) \\ \mathbf{q}_{\mathrm{I}}(t) \end{Bmatrix} = \begin{bmatrix} \mathbf{L}^{\mathrm{T}} & \mathbf{L}^{\mathrm{T}}\boldsymbol{\Gamma}^{\mathrm{T}} \\ \mathbf{0} & \boldsymbol{\Xi}^{\mathrm{T}} \end{bmatrix} \begin{Bmatrix} \hat{\mathbf{f}}_{\mathrm{B}}(t) \\ \hat{\mathbf{f}}_{\mathrm{I}}(t) \end{Bmatrix}, \tag{10}$$

where $\mathbf{M} = \mathbf{T}_{\text{L-CC}}^{\mathrm{T}}\bar{\mathbf{M}}\mathbf{T}_{\text{L-CC}}$ and $\mathbf{K} = \mathbf{T}_{\text{L-CC}}^{\mathrm{T}}\bar{\mathbf{K}}\mathbf{T}_{\text{L-CC}}$.

A single transformation matrix encompassing both the CB and L-CC MOR methods can also be derived, allowing for the straightforward representation of physical DoFs into modal ones, as follows:

$$\begin{Bmatrix} \hat{\mathbf{q}}_{\mathrm{B}}(t) \\ \hat{\mathbf{q}}_{\mathrm{I}}(t) \end{Bmatrix} = \mathbf{T} \begin{Bmatrix} \mathbf{q}_{\mathrm{B}}(t) \\ \mathbf{q}_{\mathrm{I}}(t) \end{Bmatrix} = \begin{bmatrix} \mathbf{L} & \mathbf{0} \\ \mathbf{\Gamma L} & \mathbf{\Xi} \end{bmatrix} \begin{Bmatrix} \mathbf{q}_{\mathrm{B}}(t) \\ \mathbf{q}_{\mathrm{I}}(t) \end{Bmatrix}. \tag{11}$$

Even though the flowchart depicted in Fig. 1 suggests that the reduction of interior DoFs must be carried out prior to reducing boundary equations, steps **(3)** and **(4)** are independent in the MGBMS. This means that $\mathbf{L}$ can be obtained without the need for reducing interior DoFs, for example, because Eq. (7) is solved at the unit cell's global level and not locally, as done in the GBMS [24].

2.4 A review on the one-dimensional wave-based finite element method

In this section, we delve into the mathematical formulation of the one-dimensional WFEM, encompassing the final phase shown in Fig. 1 (step **(5)**). This review primarily draws insights from [43, 44], augmented by our own experiences in applying the WFEM to various problems over the years.

2.4.1 Basic developments

The time-domain reduced EoMs derived previously, given by Eq. (10), can be written in the frequency domain as $\tilde{\mathbf{D}}^{(n)}(\omega)\mathbf{q}^{(n)}(\omega) = \mathbf{F}^{(n)}(\omega)$, where $\tilde{\mathbf{D}}^{(n)}(\omega) = -\omega^2\mathbf{M} + \mathbf{K}$ represents the unit cell's dynamic stiffness matrix, $\mathbf{q}^{(n)}(\omega)$ and $\mathbf{F}^{(n)}(\omega)$ denote displacements/rotations and forces/moments, respectively, and ω is the circular frequency. Dissipation effects (damping) due to material behavior, joints, and other sources can be accounted for by making the unit cell's stiffness matrix complex, i.e., $\mathbf{K} \rightarrow (1+\mathrm{i}\eta)\mathbf{K}$, where η stands for the hysteretic damping coefficient and i is the imaginary unit [45]. Accordingly, the unit cell DSM can be partitioned following the DoFs locations introduced before in Subsection 2.1 (cf. Fig. 2), as follows:

$$\begin{bmatrix} \tilde{\mathbf{D}}^{(n)}_{\mathrm{LL}}(\omega) & \tilde{\mathbf{D}}^{(n)}_{\mathrm{LR}}(\omega) & \tilde{\mathbf{D}}^{(n)}_{\mathrm{LI}}(\omega) \\ \tilde{\mathbf{D}}^{(n)}_{\mathrm{RL}}(\omega) & \tilde{\mathbf{D}}^{(n)}_{\mathrm{RR}}(\omega) & \tilde{\mathbf{D}}^{(n)}_{\mathrm{RI}}(\omega) \\ \tilde{\mathbf{D}}^{(n)}_{\mathrm{IL}}(\omega) & \tilde{\mathbf{D}}^{(n)}_{\mathrm{IR}}(\omega) & \tilde{\mathbf{D}}^{(n)}_{\mathrm{II}}(\omega) \end{bmatrix} \begin{Bmatrix} \mathbf{q}^{(n)}_{\mathrm{L}}(\omega) \\ \mathbf{q}^{(n)}_{\mathrm{R}}(\omega) \\ \mathbf{q}^{(n)}_{\mathrm{I}}(\omega) \end{Bmatrix} = \begin{Bmatrix} \mathbf{F}^{(n)}_{\mathrm{L}}(\omega) \\ \mathbf{F}^{(n)}_{\mathrm{R}}(\omega) \\ \mathbf{F}^{(n)}_{\mathrm{I}}(\omega) \end{Bmatrix}. \tag{12}$$

After performing some mathematical manipulations, including dynamic condensation, and DoFs and load equilibrium between neighboring unit cells (n) and $(n+1)$ of a periodic structure, one obtains (with frequency dependencies omitted from now on for convenience) [46]:

$$\mathbf{u}^{(n+1)}_{\mathrm{L}} = \mathbf{S}\mathbf{u}^{(n)}_{\mathrm{L}} + \mathbf{b}^{(n)}, \tag{13}$$

where $\mathbf{u}$, $\mathbf{S}$, and $\mathbf{b}$ are known as the unit cell's state vector, transfer matrix, and load vector, respectively, given by:

$$\mathbf{u}^{(n)}_{\mathrm{L}} = \begin{Bmatrix} \mathbf{q}^{(n)}_{\mathrm{L}} \\ -\mathbf{F}^{(n)}_{\mathrm{L}} \end{Bmatrix}, \quad \mathbf{S} = \begin{bmatrix} -\mathbf{D}^{-1}_{\mathrm{LR}}\mathbf{D}_{\mathrm{LL}} & -\mathbf{D}^{-1}_{\mathrm{LR}} \\ \mathbf{D}_{\mathrm{RL}} - \mathbf{D}_{\mathrm{RR}}\mathbf{D}^{-1}_{\mathrm{LR}}\mathbf{D}_{\mathrm{LL}} & -\mathbf{D}_{\mathrm{RR}}\mathbf{D}^{-1}_{\mathrm{LR}} \end{bmatrix}, \quad \mathbf{b}^{(n)} = \begin{Bmatrix} \mathbf{D}_{\mathrm{qI}}\mathbf{F}^{(n)}_{\mathrm{I}} \\ \mathbf{D}_{\mathrm{fI}}\mathbf{F}^{(n)}_{\mathrm{I}} - \mathbf{F}^{(n)}_{\mathrm{B}} \end{Bmatrix}, \tag{14}$$

with $\mathbf{D}_{\mathrm{qI}} = -\mathbf{D}^{-1}_{\mathrm{LR}}\mathbf{D}_{\mathrm{LI}}$ and $\mathbf{D}_{\mathrm{fI}} = \mathbf{D}_{\mathrm{RI}} - \mathbf{D}_{\mathrm{RR}}\mathbf{D}^{-1}_{\mathrm{LR}}\mathbf{D}_{\mathrm{LI}}$.

From the recurrence relation embedded in Eq. (13), one can derive the following relationships that support subsequent mathematical developments:

$$\mathbf{u}^{(n+1)}_{\mathrm{L}} = \mathbf{S}^{n}\mathbf{u}^{(1)}_{\mathrm{L}} + \sum\nolimits_{k=1}^{n} \mathbf{S}^{n-k}\mathbf{b}^{(k)}, \tag{15}$$

$$\mathbf{u}^{(N+1)}_{\mathrm{L}} = \mathbf{S}^{N+1-n}\mathbf{u}^{(n)}_{\mathrm{L}} + \sum\nolimits_{k=n}^{N} \mathbf{S}^{N-k}\mathbf{b}^{(k)}, \tag{16}$$

where N accounts for the number of unit cells of a finite periodic structure.

2.4.2 Computation of wave modes

Computing wave modes is a crucial task in the WFEM. Unfortunately, this step is highly prone to numerical issues, as reviewed in this subsection. First, the Bloch-Floquet periodicity condition for problems encompassing one-dimensional wave propagation behavior allows us to write [29]:

$$\mathbf{u}_{\mathrm{L}}^{(n+1)} = \mu \mathbf{u}_{\mathrm{L}}^{(n)}, \tag{17}$$

where $\mu = \exp(-\mathrm{i}k\Delta)$, k is the corresponding wavenumber, and Δ is the unit cell length along the direction of wave propagation. Considering external loads are zero in Eq. (13), one obtains [47]:

$$(\mathbf{S} - \mu_j \mathbf{I})\boldsymbol{\Phi}_j = \mathbf{0}. \tag{18}$$

The solution of this standard eigenvalue problem allows obtaining μ_j and $\boldsymbol{\Phi}_j \propto \mathbf{u}_{\mathrm{L}}^{(n)}$, which are called wave modes and represent the propagation constant and wave shapes, respectively. Of great interest in structural dynamics and many other areas are the so-called wavenumbers, computed as $k_j = (\ln \mu_j)/(-\mathrm{i}\Delta)$.

In general, solving Eq. (18) can be challenging, as $\boldsymbol{\Phi}_j$ collects displacements/rotations and forces/moments (cf. Eq. (14)), whose order of magnitude can be quite disparate [48, 49]. To mitigate this issue, one can resort to Zhong's eigenvalue problem [43, 50]:

$$\left(\mathbf{N}\mathbf{J}\mathbf{L}^{\mathrm{T}} + \mathbf{L}\mathbf{J}\mathbf{N}^{\mathrm{T}} - \lambda_j \mathbf{L}\mathbf{J}\mathbf{L}^{\mathrm{T}}\right)\mathbf{z}_j = \mathbf{0}, \tag{19}$$

where:

$$\mathbf{N} = \begin{bmatrix} \mathbf{D}_{\mathrm{RL}} & \mathbf{0} \\ -(\mathbf{D}_{\mathrm{LL}} + \mathbf{D}_{\mathrm{RR}}) & -\mathbf{I} \end{bmatrix}, \qquad \mathbf{L} = \begin{bmatrix} \mathbf{0} & \mathbf{I} \\ \mathbf{D}_{\mathrm{LR}} & \mathbf{0} \end{bmatrix}, \qquad \mathbf{J} = \begin{bmatrix} \mathbf{0} & \mathbf{I} \\ -\mathbf{I} & \mathbf{0} \end{bmatrix}. \tag{20}$$

Mencik and Ichchou [51] demonstrated that the eigenvalues of Eq. (19) are related to propagation constants, such that μ_j can be retrieved as $\mu_j = \frac{1}{2}\left(\lambda_j \pm \sqrt{\lambda_j^2 - 4}\right)$. Regarding the eigenvectors of the standard eigenvalue problem in Eq. (18), they can be obtained as follows [43]:

$$\boldsymbol{\Phi}_j = \begin{bmatrix} \mathbf{I} & \mathbf{0} \\ \mathbf{D}_{\mathrm{RR}} & \mathbf{I} \end{bmatrix} \mathbf{w}_j, \qquad \text{with} \qquad \mathbf{w}_j = \mathbf{J}\left(\mathbf{L}^{\mathrm{T}} - \tfrac{1}{\mu_j}\mathbf{N}^{\mathrm{T}}\right)\mathbf{z}_j. \tag{21}$$

Wave modes computed previously can then be grouped into matrices according to the direction of wave propagation, i.e., into those related to positive-going (μ_j, $\boldsymbol{\Phi}_j$) and negative-going waves (μ_j^*, $\boldsymbol{\Phi}_j^*$) [49, 52]:

$$\boldsymbol{\mu} = \mathrm{diag}(\mu_1 \;\; \mu_{...}), \quad \boldsymbol{\mu}^* = \mathrm{diag}(\mu_1^* \;\; \mu_{...}^*), \quad \boldsymbol{\Phi} = [\boldsymbol{\phi}_1 \;\; \boldsymbol{\phi}_{...}] = \begin{bmatrix} \boldsymbol{\Phi}_{\mathrm{q}} \\ \boldsymbol{\Phi}_{\mathrm{F}} \end{bmatrix}, \quad \boldsymbol{\Phi}^* = [\boldsymbol{\phi}_1^* \;\; \boldsymbol{\phi}_{...}^*] = \begin{bmatrix} \boldsymbol{\Phi}_{\mathrm{q}}^* \\ \boldsymbol{\Phi}_{\mathrm{F}}^* \end{bmatrix}, \tag{22}$$

where q and F denote the displacements/rotations and forces/moments partitions of $\boldsymbol{\Phi}$ and $\boldsymbol{\Phi}^*$, respectively.

2.4.3 Computation of forced responses due to harmonic loads

The forced response of a finite structure can be obtained by expressing the state vector and the vector of external loads as a linear combination of wave amplitudes, utilizing the computed wave modes, as follows:

$$\mathbf{u}_{\mathrm{L}}^{(n)} = \boldsymbol{\Phi}\mathbf{Q}^{(n)} + \boldsymbol{\Phi}^*\mathbf{Q}^{*(n)}, \tag{23}$$

$$\mathbf{b}^{(n)} = \boldsymbol{\Phi}\mathbf{Q}_{\mathrm{B}}^{(n)} + \boldsymbol{\Phi}^*\mathbf{Q}_{\mathrm{B}}^{*(n)}, \tag{24}$$

where $\mathbf{Q}^{(n)}$, $\mathbf{Q}^{*(n)}$, $\mathbf{Q}_{\mathrm{B}}^{(n)}$ and $\mathbf{Q}_{\mathrm{B}}^{*(n)}$ are amplitude vectors gathering amplitudes related to the wave modes' expansion of $\mathbf{u}_{\mathrm{L}}^{(n)}$ and $\mathbf{b}^{(n)}$. By manipulating Eqs. (15) and (16), one arrives at:

$$\mathbf{Q}^{(n)} = \boldsymbol{\mu}^{n-1}\mathbf{Q}^{(1)} + \sum\nolimits_{k=1}^{n-1} \boldsymbol{\mu}^{n-k-1}\mathbf{Q}_{\mathrm{B}}^{(k)}, \tag{25}$$

$$\mathbf{Q}^{*(n)} = \boldsymbol{\mu}^{N+1-n}\mathbf{Q}^{*(N+1)} - \sum\nolimits_{k=n}^{N} \boldsymbol{\mu}^{k-n+1}\mathbf{Q}_{\mathrm{B}}^{*(k)}, \tag{26}$$

with $\mathbf{Q}_{\mathrm{B}}^{(k)}$ and $\mathbf{Q}_{\mathrm{B}}^{*(k)}$ obtained after manipulating Eq. (24), expressed as:

$$\mathbf{Q}_{\mathrm{B}}^{(k)} = \left(\boldsymbol{\mu}\boldsymbol{\Phi}_{\mathrm{q}}^{*\mathrm{T}}\mathbf{D}_{\mathrm{LI}} + \boldsymbol{\Phi}_{\mathrm{q}}^{*\mathrm{T}}\mathbf{D}_{\mathrm{RI}}\right)\mathbf{F}_{\mathrm{I}}^{(k)} - \boldsymbol{\Phi}_{\mathrm{q}}^{*\mathrm{T}}\mathbf{F}_{\mathrm{B}}^{(k)}, \tag{27}$$

$$\mathbf{Q}_{\mathrm{B}}^{*(k)} = -\left(\boldsymbol{\mu}^{*}\boldsymbol{\Phi}_{\mathrm{q}}^{\mathrm{T}}\mathbf{D}_{\mathrm{LI}} + \boldsymbol{\Phi}_{\mathrm{q}}^{\mathrm{T}}\mathbf{D}_{\mathrm{RI}}\right)\mathbf{F}_{\mathrm{I}}^{(k)} + \boldsymbol{\Phi}_{\mathrm{q}}^{\mathrm{T}}\mathbf{F}_{\mathrm{B}}^{(k)}. \tag{28}$$

Once the state vector $\mathbf{u}_{\mathrm{L}}^{(n)}$ is written in terms of DoFs and loads, $\mathbf{q}_{\mathrm{L}}^{(n)}$ and $\mathbf{F}_{\mathrm{L}}^{(n)}$ (cf. Eq. (14)), and considering the partitions introduced in Eq. (22), combining Eqs. (23), (25), and (26) yields the following result:

$$\mathbf{q}_{\mathrm{L}}^{(n)} = \boldsymbol{\Phi}_{\mathrm{q}}\boldsymbol{\mu}^{n-1}\mathbf{Q} + \boldsymbol{\Phi}_{\mathrm{q}}^{*}\boldsymbol{\mu}^{N+1-n}\mathbf{Q}^{*} + \boldsymbol{\Phi}_{\mathrm{q}}\sum\nolimits_{k=1}^{n-1}\boldsymbol{\mu}^{n-k-1}\mathbf{Q}_{\mathrm{B}}^{(k)} - \boldsymbol{\Phi}_{\mathrm{q}}^{*}\sum\nolimits_{k=n}^{N}\boldsymbol{\mu}^{k+1-n}\mathbf{Q}_{\mathrm{B}}^{*(k)}, \tag{29}$$

$$-\mathbf{F}_{\mathrm{L}}^{(n)} = \boldsymbol{\Phi}_{\mathrm{F}}\boldsymbol{\mu}^{n-1}\mathbf{Q} + \boldsymbol{\Phi}_{\mathrm{F}}^{*}\boldsymbol{\mu}^{N+1-n}\mathbf{Q}^{*} + \boldsymbol{\Phi}_{\mathrm{F}}\sum\nolimits_{k=1}^{n-1}\boldsymbol{\mu}^{n-k-1}\mathbf{Q}_{\mathrm{B}}^{(k)} - \boldsymbol{\Phi}_{\mathrm{F}}^{*}\sum\nolimits_{k=n}^{N}\boldsymbol{\mu}^{k+1-n}\mathbf{Q}_{\mathrm{B}}^{*(k)}, \tag{30}$$

with $\mathbf{Q} \equiv \mathbf{Q}^{(1)}$ and $\mathbf{Q}^{*} \equiv \mathbf{Q}^{*(N+1)}$ related to wave mode amplitudes for the first (1) and fictitious $(N+1)$ unit cells of a finite periodic structure.

As the numerical simulations shown afterward have been conducted assuming the plate-type elastic metamaterial is in a "free-free" condition, for which $\mathbf{F}_{\mathrm{L}}^{(1)} = \mathbf{0}$ and $\mathbf{F}_{\mathrm{L}}^{(N+1)} = \mathbf{0}$, the following linear system of equations holds for determining $\mathbf{Q}$ and $\mathbf{Q}^{*}$:

$$\begin{bmatrix} \mathbf{I} & \boldsymbol{\Phi}_{\mathrm{F}}^{-1}\boldsymbol{\Phi}_{\mathrm{F}}^{*}\boldsymbol{\mu}^{N} \\ \boldsymbol{\Phi}_{\mathrm{F}}^{*-1}\boldsymbol{\Phi}_{\mathrm{F}}\boldsymbol{\mu}^{N} & \mathbf{I} \end{bmatrix} \begin{Bmatrix} \mathbf{Q} \\ \mathbf{Q}^{*} \end{Bmatrix} = \begin{Bmatrix} \boldsymbol{\Phi}_{\mathrm{F}}^{-1}\boldsymbol{\Phi}_{\mathrm{F}}^{*}\sum_{k=1}^{N}\boldsymbol{\mu}^{k}\mathbf{Q}_{\mathrm{B}}^{*(k)} \\ -\boldsymbol{\Phi}_{\mathrm{F}}^{*-1}\boldsymbol{\Phi}_{\mathrm{F}}\sum_{k=1}^{N}\boldsymbol{\mu}^{N-k}\mathbf{Q}_{\mathrm{B}}^{(k)} \end{Bmatrix}. \tag{31}$$

Solving this system enables the determination of any response of a periodic structure, in reduced coordinates, by considering expressions introduced in Eqs. (29) and (30), as well as relations which can be derived from Eq. (12). Physical responses can afterward be obtained by considering Eq. (11).

3 Numerical simulations

The numerical simulations presented below were conducted to demonstrate the outstanding performance of the MGBMS and WFEM in computing dispersion curves, wave shapes, and forced responses due to harmonic loads in periodic structures. In particular, the study addresses the propagation of bending waves through a plate-type EM designed to exhibit locally-resonant bandgaps.

Relevant dimensions of the considered EM are provided in Figs. 3a and 3b ($\Delta = 30\,\mathrm{mm}$), whereas the complete unit cell design, including both the bare cell and the resonator, is illustrated in Fig. 3c for convenience. The EM is assumed to be made of structural steel, for which the elastic modulus, Poisson's ratio, density, and hysteretic damping coefficient have been taken as $200\,\mathrm{GPa}$, 0.3, $7850\,\mathrm{kg\,m^{-3}}$ and $\eta = 1\%$, respectively.

Numerical simulations presented hereafter were performed between 0 Hz and 5000 Hz, using frequency increments of 5 Hz. Convergence analysis of the FE mesh of a single unit cell of the EM was conducted to ensure the reliability and accuracy of the numerical simulations within the considered frequency range. Target convergence was assumed to be achieved when the relative error between the highest natural frequencies obtained using two successive mesh refinements was less than 1%. In this context, Fig. 3d illustrates the FE mesh used for conducting numerical simulations on the EM in the following subsections. Regarding the modeling of the unit cell, it was carried out using four-noded Reissner-Mindlin plate elements, with a thickness input of 2 mm, assuming linear behavior for both material and interpolation functions.

Lastly, Fig. 3e illustrates the finite EM considered in our study, comprising a periodic system made with $N = 10$ identical unit cells. It also depicts the input and output locations, associated with the z-direction, which are used to compute forced responses later.

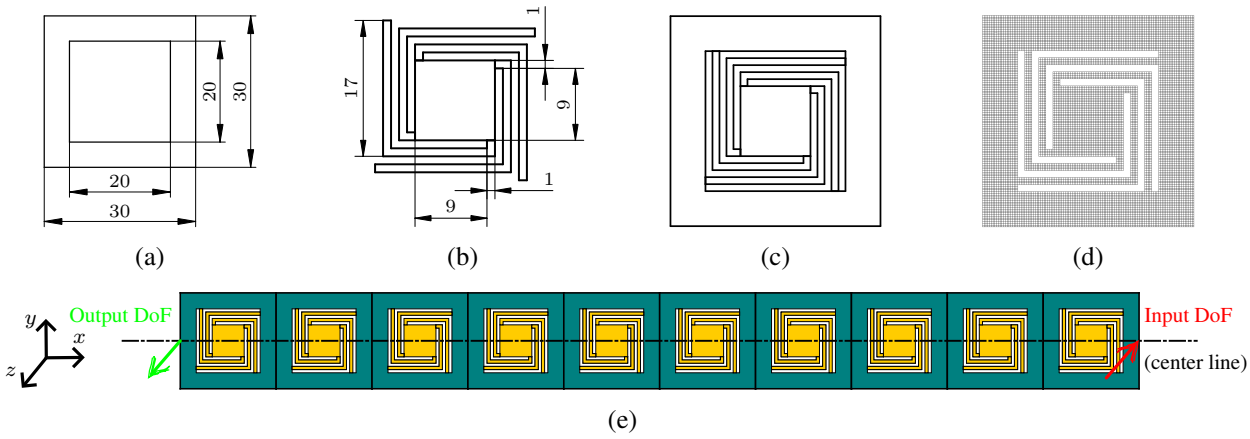

Figure 3: Details about the plate-type EM: dimensions in millimeters of the (a) bare unit cell and (b) resonator; (c) complete cell design; (d) FE mesh; and (e) EM with 10 identical cells investigated in this work.

The error between forced responses calculated by the WFEM with MGBMS ($\mathbf{H}_{\text{WFEM + MGBMS}}$) and the reference solution obtained by the FEM ($\mathbf{H}_{\text{FEM}}$) was quantified using the relative error between the j$^{\text{th}}$ resonance frequencies (f_{rj}) identified in the forced responses, measuring mass and stiffness variations, given by:

$$\text{RE}_{f_{rj}} = \frac{f_{\text{WFEM + MGBMS}_j} - f_{\text{FEM}_j}}{f_{\text{FEM}_j}}. \tag{32}$$

On the other hand, discrepancies between the amplitudes of forced responses were assessed using the Cross Signature Scale Factor (CSF) metric, calculated as follows [53]:

$$\text{CSF}(\omega) = \frac{2\left|\mathbf{H}^{\text{H}}_{\text{WFEM + MGBMS}}\mathbf{H}^{\text{T}}_{\text{FEM}}\right|}{\mathbf{H}^{\text{H}}_{\text{WFEM + MGBMS}}\mathbf{H}^{\text{T}}_{\text{WFEM + MGBMS}} + \mathbf{H}^{\text{H}}_{\text{FEM}}\mathbf{H}^{\text{T}}_{\text{FEM}}}, \tag{33}$$

where the superscript $(\ )^{\text{H}}$ denotes the Hermitian operator. This indicator ranges from zero to one and operates similarly to the MAC number, implying that a value of zero indicates that the transfer functions are completely uncorrelated, while values near one indicate a high degree of similarity between them.

Numerical simulations were conducted on a DELL XPS 8920 desktop computer equipped with an Intel(R) Core(TM) i7-7700 CPU running at 3.60 GHz and 32.0 GB of RAM. Additionally, our codes were developed in MATLAB®, and very few optimizations were implemented.

3.1 Unit cell model order reduction

The EoMs of a unit cell of the plate-type EM, given by Eq. (1), were reduced using the theory described in Subsections 2.2 and 2.3. Fixed interface modes gathered in $\boldsymbol{\Xi}$ (cf. Eq. (4)) and low-frequency eigensolutions of Eq. (7) were determined using frequency-based truncation criteria, where vibration modes with natural frequencies less than 5 and 2 times the maximum frequency of analysis were retained, respectively. Table 1 summarizes the unit cell model-size details before and after applying the MOR procedure, where significant reduction levels of boundary and internal equations are observed, with an overall reduction rate of 99.90%.

Table 1: Unit cell model-size details.

Set of equations	Full FEM (N_F)	MGBMS (N_R)	N_R/N_F (%)
Boundary	1452	52	3.58
Internal	73794	24	0.03
Complete	75246	76	0.10

3.2 Computation of dispersion curves and wave shapes

The reduced order model derived previously was then used to compute the dispersion curves illustrated in Fig. 4, which relate to xz-plane bending and twisting motion of a plate-like EM of infinite extent. The figure also depicts, in shaded areas, the bandgap frequency ranges encountered between 0 and 5000 Hz, determined using the indicator of minimal evanescence ratio [54, 55, 56]. As the geometry of the resonators favors the coupling between twisting and bending motion, wave shapes related to each branch in Fig. 4 exhibit mode conversion along the frequency range.

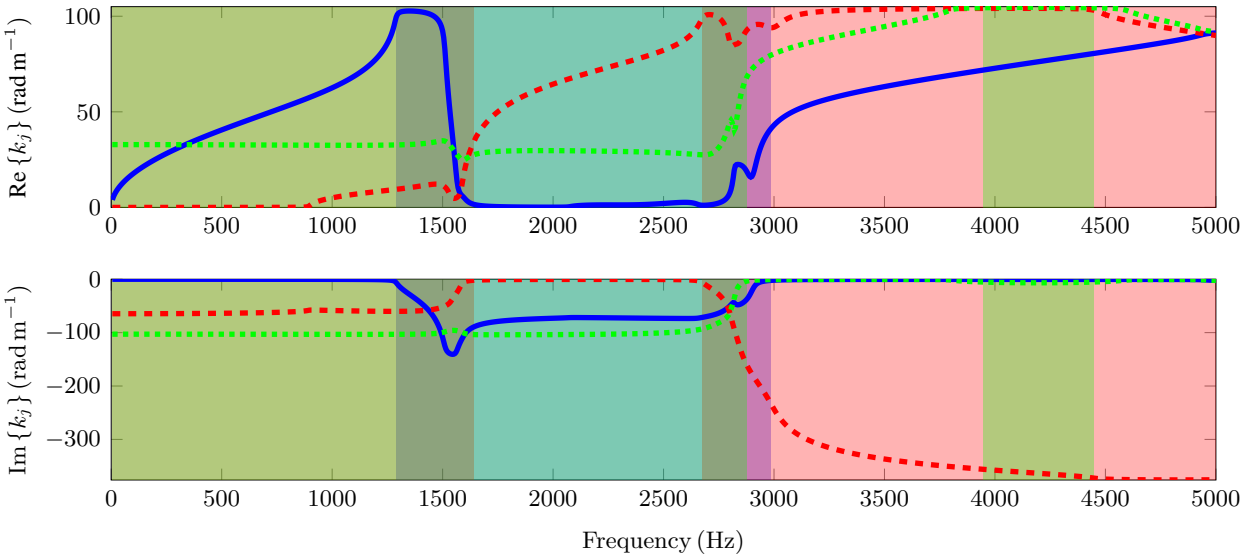

Figure 4: Dispersion curves with frequency ranges of bandgaps highlighted in lighter colors corresponding to those used to plot each curve.

Of particular interest in this study is the application of the WFEM with MGBMS to investigate the bending behavior of the EM in the xz-plane. Bandgaps affecting the bending behavior of the plate-like EM can be identified in Fig. 4 for 1290–1640 Hz, which comprise the first complete bandgap between the red dashed and blue solid lines; 2675–2875 Hz, corresponding to the second complete bandgap between the green dash-dotted and red dashed lines; and 3945–4445 Hz. To aid comprehension, Fig. 5 illustrates wave shapes for the previously seen dispersion curves, calculated for the central frequencies of each bending-related bandgap.

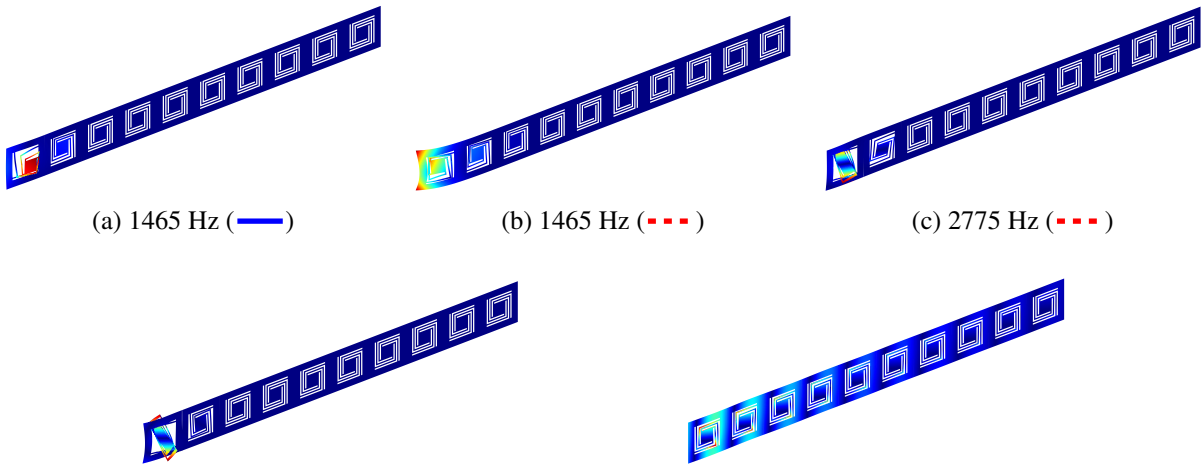

(a) 1465 Hz (——) (b) 1465 Hz (- - -) (c) 2775 Hz (- - -)

(d) 2775 Hz (·····) (e) 4195 Hz (·····)

Figure 5: Wave shapes corresponding to dispersion curves in Fig. 4, calculated for the central frequencies of each bending-related bandgap, for finite periodic structures with 10 unit cells.

3.3 Computation of forced responses due to harmonic loads

Following the steps summarized in Fig. 1, the final task in the analysis of periodic structures using the WFEM and MGBMS involves calculating forced responses of finite systems. Therefore, Fig. 6a shows frequency response functions (FRFs) calculated using the traditional FEM using the direct method and WFEM + MGBMS, considering the input and output locations depicted in Fig. 3e. Clearly, both forced responses are in very good visual agreement across the entire frequency range. Additionally, the bandgap frequency ranges determined using the Bloch-Floquet theory before (cf. Fig. (4)), highlighted in shaded gray in Fig. 6a, precisely coincide with the forbidden bands in the forced responses.

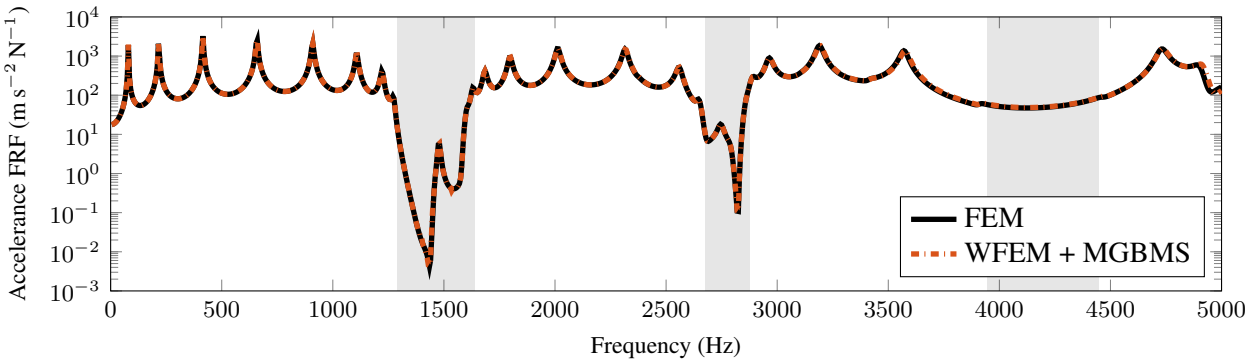

(a) Comparison between FRFs obtained by the FEM and the WFEM + MGBMS, with bandgaps highlighted in gray.

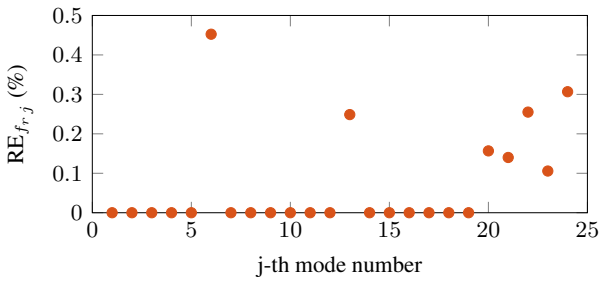

(b) Relative error.

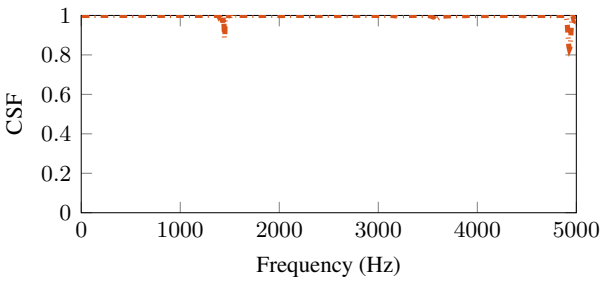

(c) Cross signature scale factor.

Figure 6: Calculation of FRFs using the FEM and WFEM + MGBMS and error evaluation.

The relative error analysis between the resonance frequencies of the reference model and the WFEM reduced one is depicted in Fig. 6b, confirming minimal frequency discrepancies in Fig. 6a. It also reveals that these discrepancies are primarily concentrated at higher frequencies, which is an expected result consistent with most MOR methods, due to the neglect of less-important high-frequency content in the MOR process. The maximum relative error identified in Fig. 6b is less than 0.5% and occurs at the 6$^{\text{th}}$ resonance frequency, being mainly attributed to the frequency discretization with increments of 5 Hz employed during simulations. The CSF values shown in Fig. 6c further support these conclusions, with values close to one across the whole frequency range. Slightly lower CSF values can be observed near 1500 Hz and 5000 Hz in Fig. 6c, indicating minimal amplitude discrepancies between the FRFs obtained by the reduced WFEM model and the full FEM one. In the former case, disparities are related to inaccuracies when calculating some high-order evanescent wave modes, whereas in the latter, they are a consequence of truncation of higher frequency modes (residual modes), as previously discussed.

Aiming to investigate the performance of the MGBMS when applied in conjunction with the WFEM compared to the traditional FEM, the computational time needed for calculating the FRFs shown in Fig. 6a is summarized in Table 2. It can be observed that most of the time required for the calculation of the forced response using WFEM + MGBMS is related to the reduction of interior DoFs by employing the CB MOR method. This involves solving an eigenvalue problem necessary to assemble the matrix of fixed interface modes $\boldsymbol{\Xi}$ and performing a system solution to find the matrix of constraint modes $\boldsymbol{\Gamma}$ (cf. Eqs. (4) and (5)). Time related to data reading and matrix manipulations, denoted by the task “Other” in Table 2, is the next

on the list. It should be pointed out that this category does not include the generation of the FE model of the unit cell or the export process of related EoMs. The remaining tasks involve negligible computational effort, which includes the computation of wave modes ($(\boldsymbol{\mu}, \boldsymbol{\Phi})$ and $(\boldsymbol{\mu}^*, \boldsymbol{\Phi}^*)$), reduction of boundary DoFs using the L-CC MOR technique, calculation of wave mode amplitudes ($\mathbf{Q}$ and $\mathbf{Q}^*$) utilizing Eq. (31), and evaluation of physical responses.

Table 2: Timing data in seconds related to the calculation of the magnitudes of FRFs depicted in Fig. 6a.

	CB MOR	L-CC MOR	Computation of wave modes	Calculation of wave mode amplitudes	Post-processing: evaluation of physical DoFs	Other	Total
Related equations	(4)–(5)	(6)–(11)	(19)–(22)	(31)	(29)–(30), (12), (11)	-	-
WFEM + MGBMS	91.54	5.94	6.33	2.12	0.35	10.92	117.20
FEM	-	-	-	-	9539.00	-	9539.00

Lastly, Table 2 also shows that when the CB and L-CC MOR methods are combined with the standard WFEM, considerable time reduction is achieved for evaluating forced responses of a finite periodic system compared to the traditional FEM. In particular, the analysis of the plate-type EM using the WFEM + MGBMS is approximately 82 times faster compared to the FEM. This result seems very promising for obtaining an harmonic deformation pattern of the complete EM, since one would need to evaluate a maximum of $N \times 75246 = 752460$ responses, related to the physical DoFs of the structure, which would require approximately $0.35/1000 \times 752460 \approx 260\,\mathrm{s}$ to obtain a deformation pattern related to a given frequency.

4 Concluding remarks

In this work, we demonstrate the use of the MGBMS and WFEM for the efficient and accurate modeling of periodic structures. Internal and boundary DoFs of a unit cell were reduced using the CB and L-CC MOR methods, respectively. In the latter case, the reduction of boundary DoFs was performed respecting the application of the Bloch-Floquet theorem. Simulations have demonstrated the outstanding performance of size-reduced unit cell models, with only 0.10% of modal DoFs, for analyzing periodic systems using the WFEM. Relative errors between resonance frequencies identified in FRFs using the WFEM + MGBMS and the FEM were less than 0.5%, indicating good accuracy of the reduced modal model in terms of mass and stiffness matrices. Amplitude discrepancies were evaluated using the CSF, with values approaching one in the entire frequency range, confirming the remarkable performance of the proposed modeling approach.

Acknowledgements

V. M. S. Santos acknowledges the São Paulo Research Foundation (FAPESP) for the grants #2023/11207-7 and #2024/07549-2, and the Brazilian Coordination for the Improvement of Higher Education Personnel (CAPES). V. M. S. Santos and T. P. Sales are grateful to the FAPESP for its support to the thematic grant #2018/15894-0, related to the "Periodic structure design and optimization for enhanced vibroacoustic performance: ENVIBRO" research project. M. Ouisse acknowledges the graduate school EIPHI (project ANR-17-EURE-0002).

References

[1] V. F. Almeida, V. D. Lima, and J. R. F. Arruda, "Applying the phononic crystal concept to the intake muffler of a refrigeration compressor," *Appl. Acoust.*, vol. 194, p. 108800, 2022.

[2] R. B. Santos, G. Berres, D. J. Inman, C. G. Gonsalez-Bueno, and D. D. Bueno, "A practical approach to evaluate periodic rods composed of cells with geometric and material periodicity," *J. Sound Vib.*, vol. 553, p. 117646, 2023.

[3] T. Vasileiadis, J. Varghese, V. Babacic, J. Gomis-Bresco, D. Navarro Urrios, and B. Graczykowski, "Progress and perspectives on phononic crystals," *J. Appl. Phys.*, vol. 129, no. 16, 2021.

[4] M. Oudich, N. J. R. K. Gerard, Y. Deng, and Y. Jing, "Tailoring Structure-Borne Sound through Bandgap Engineering in Phononic Crystals and Metamaterials: A Comprehensive Review," *Adv. Funct. Mater.*, vol. 33, no. 2, 2022.

[5] T.-T. Wang, Y.-F. Wang, Z.-C. Deng, V. Laude, and Y.-S. Wang, "Reconfigurable waveguides defined by selective fluid filling in two-dimensional phononic metaplates," *Mech. Syst. Signal Pr.*, vol. 165, p. 108392, 2022.

[6] L. Ning, Y.-Z. Wang, and Y.-S. Wang, "Active control cloak of the elastic wave metamaterial," *Int. J. Solids Struct.*, vol. 202, pp. 126–135, 2020.

[7] G. Lee, J. Park, W. Choi, B. Ji, M. Kim, and J. Rho, "Multiband elastic wave energy localization for highly amplified piezoelectric energy harvesting using trampoline metamaterials," *Mech. Syst. Signal Pr.*, vol. 200, p. 110593, 2023.

[8] M. Badreddine Assouar, M. Senesi, M. Oudich, M. Ruzzene, and Z. Hou, "Broadband plate-type acoustic metamaterial for low-frequency sound attenuation," *Appl. Phys. Lett.*, vol. 101, no. 17, 2012.

[9] Z. Jia, Z. Sun, Q. Tian, Y. Luo, X. Zhang, S. Zhao, and Z. Kang, "Optimization design of all-angle negative refraction phononic crystals at a specified frequency," *Mech. Syst. Signal Pr.*, vol. 205, p. 110824, 2023.

[10] K. Yi, M. Ouisse, E. Sadoulet-Reboul, and G. Matten, "Active metamaterials with broadband controllable stiffness for tunable band gaps and non-reciprocal wave propagation," *Smar. Mat. St.*, vol. 28, no. 6, p. 065025, 2019.

[11] H. Wang, Y. Xu, P. Genevet, J.-H. Jiang, and H. Chen, "Broadband mode conversion via gradient index metamaterials," *Sci. Rep.*, vol. 6, no. 1, 2016.

[12] C. Sugino, Y. Xia, S. Leadenham, M. Ruzzene, and A. Erturk, "A general theory for bandgap estimation in locally resonant metastructures," *J. Sound Vib.*, vol. 406, pp. 104–123, 2017.

[13] T.-T. Wang, Y.-F. Wang, Z.-C. Deng, V. Laude, and Y.-S. Wang, "Reconfigurable coupled-resonator acoustoelastic waveguides in fluid-filled phononic metaplates," *Compos. Struct.*, vol. 303, p. 116355, 2023.

[14] L. Xiao, O. S. Bursi, M. Wang, S. Nagarajaiah, F. Sun, and X.-L. Du, "Metamaterial beams with negative stiffness absorbers and rotation: band-gap behavior and band-gap merging," *Eng. Struct.*, vol. 280, p. 115702, 2023.

[15] S. Ahsani, R. Boukadia, C. Droz, C. Claeys, E. Deckers, and W. Desmet, "Diffusion based homogenization method for 1D wave propagation," *Mech. Syst. Signal Pr.*, vol. 136, p. 106515, 2020.

[16] C. Yang, K. Kaynardag, and S. Salamone, "Investigation of wave propagation and attenuation in periodic supported rails using wave finite element method," *Acta Mech.*, vol. 235, pp. 1453–1469, 2023.

[17] E. J. P. d. Miranda Jr. and J. M. C. D. Santos, "Flexural Wave Band Gaps in Phononic Crystal Euler-Bernoulli Beams Using Wave Finite Element and Plane Wave Expansion Methods," *Mater. Res.*, vol. 20, no. Suppl 2, pp. 729–742, 2018.

[18] V. F. D. Poggetto and A. L. Serpa, "Elastic wave band gaps in a three-dimensional periodic metamaterial using the plane wave expansion method," *Int. J. Mech. Sci.*, vol. 184, p. 105841, 2020.

[19] V. Romero-García, J. V. Sánchez-Pérez, and L. M. Garcia-Raffi, "Propagating and evanescent properties of double-point defects in sonic crystals," *New J. Phys.*, vol. 12, no. 8, p. 083024, 2010.

[20] L. F. C. Schalcher, J. M. C. D. Santos, and E. J. P. Miranda, "Extended plane wave expansion formulation for 1-D viscoelastic phononic crystals," *Partial Differ. Equ. Appl.*, vol. 7, p. 100489, 2023.

[21] U. Lee, *Spectral Element Method in Structural Dynamics*. Wiley, 2009.

[22] J. F. Doyle, *Wave Propagation in Structures*. Springer International Publishing, 2021.

[23] D. Krattiger and M. I. Hussein, "Bloch mode synthesis: Ultrafast methodology for elastic band-structure calculations," *Phys. Rev. E*, vol. 90, no. 6, p. 063306, 2014.

[24] D. Krattiger and M. I. Hussein, "Generalized Bloch mode synthesis for accelerated calculation of elastic band structures," *J. Comput. Phys.*, vol. 357, pp. 183–205, 2018.

[25] C. Droz, R. Boukadia, and W. Desmet, "A multi-scale model order reduction scheme for transient modelling of periodic structures," *J. Sound Vib.*, vol. 510, p. 116312, 2021.

[26] W. Wang and A. V. Amirkhizi, "Reduced Order Modeling of Dynamic Mechanical Metamaterials for Analysis of Infinite and Finite Systems," *J. Appl. Mech.*, vol. 90, no. 9, 2023.

[27] Y. Fan, C. W. Zhou, J. P. Laine, M. Ichchou, and L. Li, "Model reduction schemes for the wave and finite element method using the free modes of a unit cell," *Comput. Struct.*, vol. 197, pp. 42–57, 2018.

[28] D. Jiang, S. Zhang, Y. Li, B. Chen, and N. Li, "A hybrid Bloch mode synthesis method based on the free interface component mode synthesis method," *J. Comput. Phys.*, vol. 496, p. 112556, 2024.

[29] J.-M. Mencik, "On the low- and mid-frequency forced response of elastic structures using wave finite elements with one-dimensional propagation," *Comput. Struct.*, vol. 88, no. 11–12, pp. 674–689, 2010.

[30] W. C. Hurty, "Vibrations of Structural Systems by Component Mode Synthesis," *J. Eng. Mech. Div.*, vol. 86, no. 4, pp. 51–69, 1960.

[31] R. R. Craig and M. C. C. Bampton, "Coupling of substructures for dynamic analyses." *AIAA J.*, vol. 6, no. 7, pp. 1313–1319, 1968.

[32] A. Aladwani, "A refined Bloch mode synthesis framework for fast and accurate analysis of electroelastic metamaterials with piezoelectric resonant shunt damping," *Mech. Syst. Signal Pr.*, vol. 180, p. 109380, 2022.

[33] A. Aladwani, M. Nouh, and M. I. Hussein, "State-space Bloch mode synthesis for fast band-structure calculations of non-classically damped phononic materials," *Comput. Method. Appl. M.*, vol. 396, p. 115018, 2022.

[34] L. Van Belle, N. G. R. M. Filho, M. C. Villanueva, C. Claeys, E. Deckers, F. Naets, and W. Desmet, "Fast metamaterial design optimization using reduced order unit cell modeling," in *Proc. of ISMA/USD 2020*, 2020, pp. 2487–2502.

[35] V. Cool, F. Naets, L. Van Belle, W. Desmet, and E. Deckers, "Accelerated dispersion curve calculations for periodic vibro-acoustic structures," *Front. Mech. Eng.*, vol. 8, 2022.

[36] C. Xi and H. Zheng, "Improving the generalized Bloch mode synthesis method using algebraic condensation," *Comput. Method. Appl. M.*, vol. 379, p. 113758, 2021.

[37] V. Cool, L. Van Belle, C. Claeys, E. Deckers, and W. Desmet, "Impact of the Unit Cell Choice on the Efficiency of Dispersion Curve Calculations Using Generalized Bloch Mode Synthesis," *J. Vib. Acoust.*, vol. 144, no. 2, 2021.

[38] L. Van Belle, C. Claeys, E. Deckers, and W. Desmet, "Fast forced response calculations of finite metamaterial plates using a Generalized Bloch Mode Synthesis based sub-structuring approach," in *Proc. of Euronoise*, 2021, pp. 1323–1332.

[39] X. Zhu, C. Xi, and H. Zheng, "An improvement of generalized Bloch mode synthesis method-based model order reduction technique for band-structure computation of periodic structures," *Comput. Struct.*, vol. 281, p. 107013, 2023.

[40] J.-M. Mencik, "A wave finite element approach for the analysis of periodic structures with cyclic symmetry in dynamic substructuring," *J. Sound Vib.*, vol. 431, pp. 441–457, 2018.

[41] R. J. Guyan, "Reduction of stiffness and mass matrices," *AIAA J.*, vol. 3, no. 2, pp. 380–380, 1965.

[42] N. M. M. Maia, J. M. M. e Silva, J. He, N. A. J. Lieven, R. M. Lin, G. W. Skingle, W.-M. To, and A. P. V. Urgueira, *Theoretical and Experimental Modal Analysis*. Research Studies Press LTD., 1997.

[43] J.-M. Mencik and D. Duhamel, "A wave-based model reduction technique for the description of the dynamic behavior of periodic structures involving arbitrary-shaped substructures and large-sized finite element models," *Finite Elem. Anal. Des.*, vol. 101, pp. 1–14, 2015.

[44] T. Hoang, D. Duhamel, and G. Foret, "Wave finite element method for waveguides and periodic structures subjected to arbitrary loads," *Finite Elem. Anal. Des.*, vol. 179, p. 103437, 2020.

[45] J. M. Renno and B. R. Mace, "On the forced response of waveguides using the wave and finite element method," *J. Sound Vib.*, vol. 329, no. 26, pp. 5474–5488, 2010.

[46] V. M. S. Santos, "Numerical Investigation of Wave Propagation in Beams Coupled to Metastructures Combining Spectral and Wave-Finite Element Methods," Master's thesis, Aeronautics Institute of Technology, 2022.

[47] B. R. Mace, D. Duhamel, M. J. Brennan, and L. Hinke, "Finite element prediction of wave motion in structural waveguides," *J. Acoust. Soc. Am.*, vol. 117, no. 5, pp. 2835–2843, 2005.

[48] J.-M. Mencik, "New advances in the forced response computation of periodic structures using the wave finite element (WFE) method," *Comput. Mech.*, vol. 54, no. 3, pp. 789–801, 2014.

[49] Y. Waki, B. R. Mace, and M. J. Brennan, "Numerical issues concerning the wave and finite element method for free and forced vibrations of waveguides," *J. Sound Vib.*, vol. 327, no. 1–2, pp. 92–108, 2009.

[50] W. X. Zhong and F. W. Williams, "On the direct solution of wave propagation for repetitive structures," *J. Sound Vib.*, vol. 181, no. 3, pp. 485–501, 1995.

[51] J.-M. Mencik and M. N. Ichchou, "Multi-mode propagation and diffusion in structures through finite elements," *Eur. J. Mech. A. Solids*, vol. 24, no. 5, pp. 877–898, 2005.

[52] D. Duhamel, B. R. Mace, and M. J. Brennan, "Finite element analysis of the vibrations of waveguides and periodic structures," *J. Sound Vib.*, vol. 294, no. 1–2, pp. 205–220, 2006.

[53] T. A. N. Silva, N. M. M. Maia, and J. I. Barbosa, "A model updating technique based on FRFs for damped structures," in *Proc. of ISMA/USD 2012*, 2012, pp. 2213–2226.

[54] M. Collet, M. Ouisse, M. Ruzzene, and M. N. Ichchou, "Floquet–Bloch decomposition for the computation of dispersion of two-dimensional periodic, damped mechanical systems," *Int. J. Solids Struct.*, vol. 48, no. 20, pp. 2837–2848, 2011.

[55] R. G. Salsa Junior, T. d. P. Sales, and D. A. Rade, "Optimization of Vibration Band Gaps in Damped Lattice Metamaterials," *Lat. Am. J. Solids Stru.*, vol. 20, no. 6, 2023.

[56] V. Santos, T. Sales, and M. Ouisse, "On the dynamic behavior of a one-dimensional metamaterial possessing inertial amplification mechanism combined with negative stiffness absorbers," in *Proc. 27th Int. Congr. Mech. Eng.*, 2023, pp. 1–10.